International Journal of Mass Spectrometry 287 (2009) 58–69

Contents lists available at ScienceDirect

International Journal of Mass Spectrometry

journal homepage: www.elsevier.com/locate/ijms

Profiling of phospholipids and related lipid structures using multidimensional ion mobility spectrometry-mass spectrometry

Sarah Trimpin[a,*], Bo Tan[b], Brian C. Bohrer[a], David K. O'Dell[b], Samuel I. Merenbloom[a], Mauricio X. Pazos[b], David E. Clemmer[a], J. Michael Walker[b,1]

[a] Department of Chemistry, Indiana University, Bloomington, IN 47405, United States
[b] Gill Center for Biomolecular Science and the Department of Psychological and Brain Sciences, Indiana University, Bloomington, IN 47405, United States

ARTICLE INFO

Article history:
Received 29 July 2008
Received in revised form
24 November 2008
Accepted 3 December 2008
Available online 8 January 2009

This work was presented in parts at the 56th ASMS Conference on Mass Spectrometry & Allied Topics, June 2008

Keywords:
Ion mobility spectrometry-mass spectrometry
Low-abundance
Signaling molecules
Pain
Endocannabinoid-like lipids

ABSTRACT

Increasingly comprehensive questions related to the biosynthesis of lipids relevant to understanding new signaling pathways have created daunting tasks for their chemical analysis. Here, ion mobility spectrometry (IMS) and mass spectrometry (MS) techniques combined with electrospray ionization have been used to examine mixtures of closely related lipid structures. The drift time distributions of sphingomyelins show baseline separations for ethylene chain length differences ($\Delta \sim 1.2$ ms) and partial separations in single unsaturation differences ($\Delta \sim 0.3$ ms) revealing that the most compact structures are observed with shorter chains and increasing unsaturation. Drift time distributions of different ionizations frequently fall into families with the same drift times (isodrifts) indicating that the ion attached to the lipid has little structural influence. The present data show that phospholipids, especially phosphatidylinositol, aggregate to form inverted micelles. Phospholipids (phosphatidylglycerol, phosphatidylcholine, phosphatidylethanolamine, sphingomyelin, and phosphatidylinositol) are effectively separated according to their polar head groups. This method also provides information about the mixture composition of the chemically different lipids *N*-palmitoyl glycine, *N*-arachidonoyl ethanolamide, and phosphatidylcholine existing over an array of charge states and sizes (inverted micelles) depending on mixture concentration. Multidimensional IMS^3-MS introduces an additional dimension to fragmentation analysis by separating the fragmented ions into groups related to size, shape and charge and allows determination of *sn*-1 and *sn*-2 substitution as is shown for phosphatidylglycerols. This contribution provides evidence for extending the targeted approach to global lipidomics analysis using the high-efficiency gas-phase separation afforded by multidimensional IMS-MS.

1. Introduction

The identification and biological characterization of novel lipids [1–9], greatly depends on developments in mass spectrometry (MS). These developments gave rise to the field of lipidomics, one goal of which is the identification of all endogenous lipids in an effort to elucidate new signaling cascades. Recent lipidomics approaches targeting putative endogenous *N*-acyl amino acids utilizing commercial high resolution mass spectrometers and a custom-built program for database searching of *m*/*z* fingerprints characterized 58 novel and 8 previously identified endogenous *N*-acyl amino acids from rodent and bovine nervous tissue [10,11].

Despite these achievements, MS methods are limited to measuring only ion intensity and mass-to-charge (*m*/*z*) ratios thus providing indirect information related to structure. Additional structural information is frequently obtained through a combination of techniques such as nuclear magnetic resonance spectroscopy, liquid chromatography (LC), and multidimensional MS [1–21]. The differentiation of isomers is often difficult even using hyphenated LC-MS^n approaches [10,11,22–24]. Challenges are also encountered when using electrospray ionization (ESI) because of ionization suppression and chemical background which cause information loss due to convolution of lipid complexity, insufficient ionization, and poor sensitivity for certain lipids [25–27].

Abbreviations: PALGly, *N*-palmitoyl glycine; AEA, *N*-Arachidonoyl ethanolamide, anandamide; AEA, Phospholipids; PG, Phosphatidylglycerol; PC, Phosphatidylcholine; PL, Phosphatidylinositol; PE, Phosphatidylethanolamine; SM, Sphingomyelin; 1-pal-2-ol glycerolDAG, 1-palmitoyl-2-oleoyl-sn-glycerol.

* Corresponding author at: Current address: Department of Chemistry, Wayne State University, 5101 Cass Ave., Detroit, MI 48202, United States.
Tel.: +1 313 577 9823; fax: +1 313 577 8822.
E-mail addresses: strimpin@chem.wayne.edu, sarah.trimpin@gmail.com (S. Trimpin).

[1] Deceased Jan. 5, 2008.

1387-3806/$ – see front matter © 2008 Elsevier B.V. All rights reserved.
doi:10.1016/j.ijms.2008.12.020

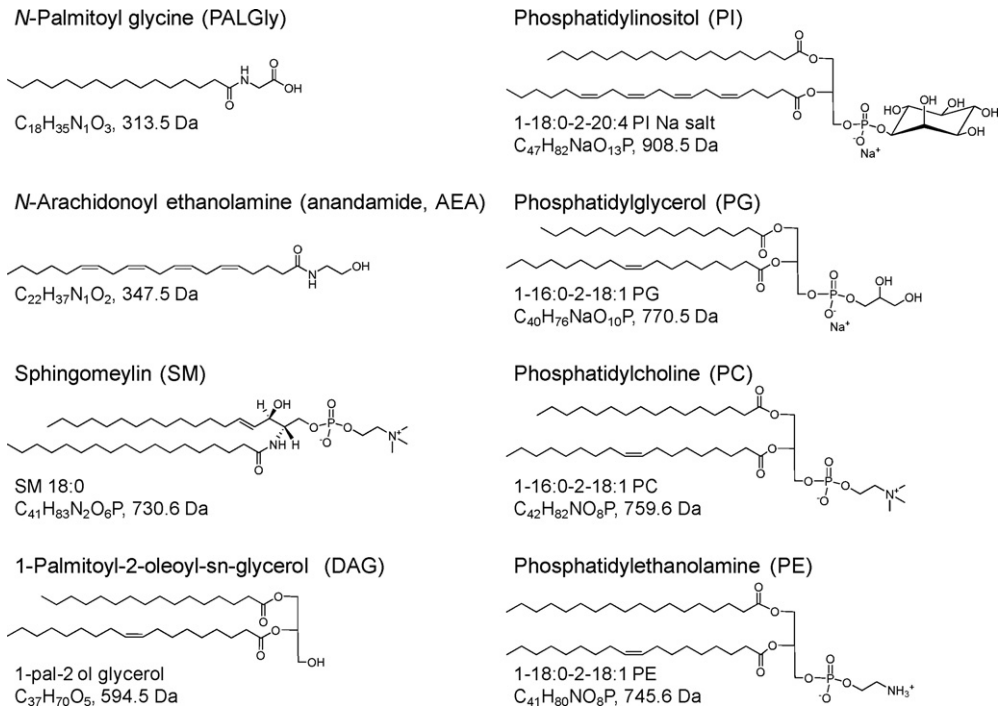

Scheme 1. Structures of *N*-acyl amino acids and related compounds. Phospholipids and anadamide are precursor molecules to *N*-acyl amino acids. 1-Palmitoyl-2-oleoyl-sn-glycerol is a defined lipid compound. The phospholipids are all mixtures of different chain lengths and unsaturations.

Matrix-assisted laser desorption/ionization (MALDI), with often superb sensitivity and high throughput capabilities [28–30], finds similar limitations [31,32], particularly at low m/z where background interferences can be significant, thus allowing other laser desorption methods to become attractive choices [33]. For example, a matrix-ionization laser desorption method showed remarkable reduction in background and permitted the elucidation of the localization of the double bond position(s) of fatty acids utilizing charge-remote fragmentation (CRF) on a commercial time-of-flight (TOF)/TOF instrument [17]. The fundamental importance of relating molecular structure to understanding biosynthetic pathways [34–37] and the need for rapid analysis of structurally, chemically, and dynamically complex systems has led to a search for novel means of characterizing lipid compositions on a molecular level.

Recently, we reported the analysis of complex materials including human plasma [38] and synthetic polymers [39] based on gas-phase separation using ESI-ion mobility spectrometry (IMS) MS. The output of the joint measurements is a multidimensional separation that contains IMS drift time (t_d, in ms) and MS data (m/z, in ns) displayed in a nested fashion $t_d(m/z)$ with a false color image of ion abundances providing a three-dimensional (3D) image. This high-efficiency separation coupled to MS detection requires only a few milliseconds revealing detailed molecular makeup. Closely related structures, even as mixtures of structural isomers, are readily discerned with IMS-MS by exploiting differences in molecular shapes, sizes, and abundances [39]. Similar IMS-MS instrumentation have been developed by different groups but only a few applications have been aimed at small molecule analysis [40–42].

Here, we demonstrate the utility of multidimensional IMS-MS for lipid analysis providing a detailed view of molecular components in chemical, structural, and dynamic complex mixtures that is based on a combined analysis of the 3D geometries and masses of lipid components adducted with cations in the gas-phase. Examples (Scheme 1) focus on the characterization of phospholipids and *N*-arachidonoyl ethanolamide (anandamide, AEA), precursor molecules to *N*-acyl amino acids [2,5,10,11], and reveal the ability to distinguish structural isomers. Additional examples are provided showing the detection of low-abundance, ionization-retarded *N*-acyl amino acids in the presence of higher-abundant mixture components such as phosphatidylcholine. Multidimensional IMS^3-MS methodology expands the abilities for obtaining mass measurements with great efficiencies from a targeted lipidomics analysis into areas with significantly increased complexity, as is the case in global lipidomics analysis, while the analytical information for challenging *N*-acyl amino acid lipids is maintained.

2. Experimental

2.1. Materials

Chloroform, tetrahydrofuran, dichloromethane, 2-butyl alcohol, and HPLC grade methanol were purchased from VWR International, Plainview, NY. Mass spectrometry/HPLC grade ammonium acetate, glycine ethyl ester hydrochloride, and LiOH were purchased from Sigma-Aldrich (St. Louis, MO). HPLC grade water was purified to a quality of $\geq$18.0 MΩ cm (e.g., Milli-Q system, Millipore, Billerica, MA, USA). Palmitic acid was purchased from Nu-Chek Prep (Elysian, MN). *N*-arachidonoyl ethanolamide (anandamide, AEA) was purchased from Cayman chemical, Ann Arbor, Michigan. Sphingomeylin (brain; SM), phosphatidylcholine (brain; PC), phosphatidylethanolamine (egg; cephalin, PE), phosphatidylinositol (soybean; PI), phosphatidylglycerol (egg; PG), and 1-palmitoyl-2-oleoyl-sn-glycerol (1-pal-2-ol glycerol, DAG) were purchased from Avanti polar lipids Inc., Alabaster, Alabama.

2.2. Synthesis of N-acyl amino acid

N-Palmitoyl glycine (PALGly) was synthesized as previously reported [9].

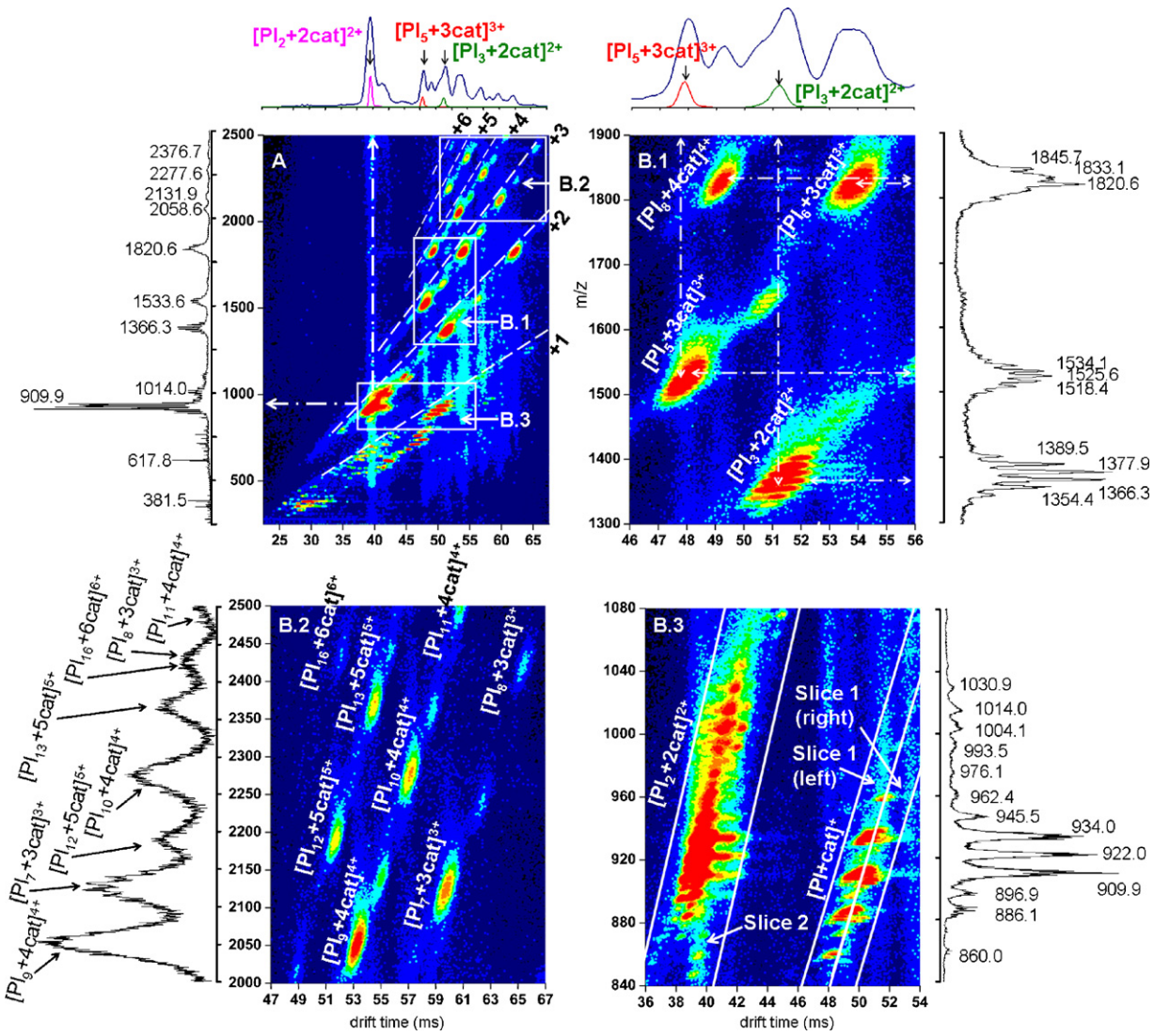

Fig. 1. Images, total mass spectra (to the left or right), and drift time distributions (on top) of phosphatidylinositols (PI). Note that the total mass spectrum provides ion abundance of all ions detected in the respective mass range as would be the case without the use of IMS. For example, the mass range of m/z 800–1100 is therefore a convolution of PI ions with charge type and aggregation states $[PI+cat]^+$, $[PI_2+2cat]^{2+}$, and $[PI_3+3cat]^{3+}$. (A) Full range image: many different charge states exist and are perhaps best described as inverted micelles. (B.1) to B.3) Inset range image: display of different charge states.

2.3. Sample preparation and introduction

Lipids were dissolved in 100% methanol with 1 mM ammonium acetate. The initial lipid concentration of each of the individual solutions was 0.35 mM AEA, 17.5 mM PalGly, 34 mM SM, 26.3 mM PC, 17 mM PE, 3.66 mM PI, and 13 mM PG. To reduce aggregation, samples were diluted between 10–10,000 times. Electrospray ionization was employed for the production of ions. For sample introduction of lipid samples, a PEEK microtee was used for connecting syringe, capillary tip, and platinum electrode, and the flow rate was set at 0.25 μL min^{-1} by the syringe pump (KD Scientific, Holliston, MA). The lipid mixtures were electrosprayed through a pulled capillary tip (75 μm i.d. × 360 μm o.d.) held at a voltage of about 5 kV.

2.4. General description to IMS-MS

A home-built instrument was used which combines electrospray ionization (ESI) with ion mobility spectrometry (IMS) and mass spectrometry (MS) [38,39,43–47]. This instrument incorporates three consecutive drift tubes that are each ~1 m in length (D1, D2, and D3), four ion funnels (F1, F2, F3, and F4), three ion gates (G1, G2, and G3), and three ion activation regions (IA1, IA2, and IA3). We describe peak positions using the nomenclature previously introduced as nested drift time (flight time) data in units of $t_d(m/z)$, where the value of t_d is given in ms [38,39,46]. Slicing software written in-house was used for data processing in conjunction with the Origin® software 6.1 and 7.0 (OriginLab Corporation, Northampton, MA 01060) used for plotting the images.

2.5. IMS-MS for separating lipid ions

The instrument can be operated in several different modes. Operating all drift regions and funnels (F2–F4) in transmission mode records the nested IMS-MS datasets by which ions exiting the drift tube through an interface region are focused into the source region of an orthogonal reflectron TOF mass spectrometer. This is possible because the flight times of the ions in the evacuated mass spectrometer (order of ns) are much shorter than drift times (order of ms) through the buffer gas. The instrument mass errors are expected to be within ±0.5 Da.

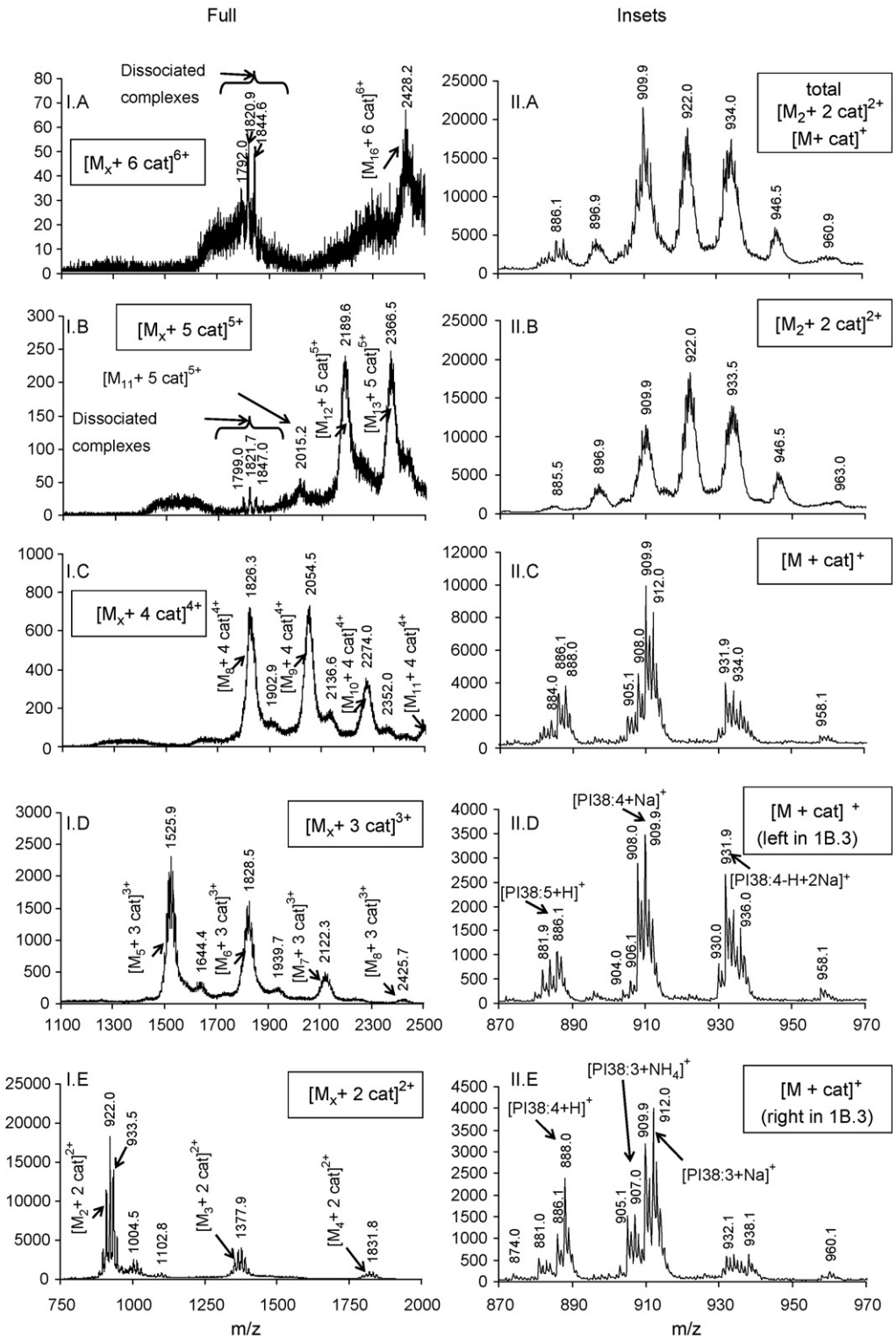

Fig. 2. Mass spectra of several charge-state families of phosphatidylinositol (PI) micelles. The mass spectrum obtained by integration along a diagonal in the t_d(m/z) distribution is used to generate slices in the *m*/*z* dimension for charge-state families ranging from the +6 series (slice 6, (I.A)) to the +1 series (slice 6, (II.C)). Some less prominent features assigned as dissociated complexes (I.A, I. B) in the charge-state resolved mass spectra indicate fragmentation of higher charge-state complexes. M_x indicates aggregation for each respective charge state.

2.6. Multidimensional IMS-MS for structural elucidation of lipid ions

For multidimensional IMS-MS, ions of specified mobilities are selected at G2 to provide mobility-selected precursor ions (Δ0.2 ms) that can be activated at IA2 for dissociation of aggregates or fragment ion analysis of covalently cleaved bonds in the respective activation regions (supply of high voltages ~200–220 V). Dissociated complexes or fragment ions of such an IMS-IMS-MS (IMS^2-MS) experiment are separated from each other as well as from the parent precursor ion in the remaining length of the drift tube and detected by the TOF-MS system. This instrument also

permits, with the additional ion funnel and drift tube segment, repeating the selection at G3 and fragmentation or dissociation in case of complexes at IA3 to provide the ability to perform IMS^3-MS experiments.

3. Results and discussion

3.1. General characterization of aggregates

The IMS-MS analyses of lipids lead to several interesting trends related to size and charge-state distributions. Phosphatidylinositols (PI) showed intense aggregation with features up to $[PI_{16}+6cat]^{6+}$ (Fig. 1). This dataset is visually remarkable in that the charge states running diagonally through the image are baseline resolved for the entire PI sample, even for isobaric compositions, e.g., $[(PI)_4+2cat]^{2+}$, $[(PI)_6+3cat]^{3+}$, vs. $[(PI)_8+4cat]^{4+}$.

Problems associated with charge-state convolution can perhaps best be seen in Fig. 1B.1 by viewing the total mass spectrum (right) for the inset region 46(1300)–56(1900). A total mass spectrum provides mass spectral data without the use of the drift time dimension and is therefore the output one would receive with MS instrumentation alone. The total mass spectrum (Inset, m/z 1300–1900) shows signals with good intensities, however, only two out of the three aggregates ($m/z \sim$ 1350–1390 and ~1518–1534) provide partially resolved signals. The total mass spectra for the respective ions at $m/z \sim$ 1775–1850 are not resolved at all. The differences in m/z between the individual signals in each of the resolved ions indicate that $m/z \sim$ 1518–1534 represents a higher charge-state aggregate than $m/z \sim$ 1350–1390. Because of possible convolution of different chain lengths (Δ 24 Da), unsaturation, and ionization (H^+, Na^+, NH_4^+, etc.) the mass spectral data alone does not permit unequivocal assignments of these aggregates. Charge-state distributions $z = 1$ through 6 are resolved in the IMS-MS image, and aggregation can be readily assigned to $[(PI)_3+2cat]^{2+}$ and $[(PI)_5+3cat]^{3+}$ by making use of the pictorial display in the IMS-MS output.

Additionally, the ions at $m/z \sim$ 1775–1850 are not resolved because of charge-state convolution as one can readily see in the IMS-MS pictorial. The assignments based on just the total drift time distribution, displayed above the IMS-MS image in Fig. 1B.1, would also be difficult due to convolution. From the IMS-MS output, however, these ions are readily assigned to charge states $[(PI)_6+3cat]^{3+}$ and $[(PI)_8+4cat]^{4+}$ by making use of the two-dimensionality of t_d and m/z.

Some insight into the pattern of features comes from taking diagonal slices (see Fig. 1A and B.3 for the location of the respective slices) through the dataset used to obtain mass spectra over a $t_d(m/z)$ range. Ten such slices are shown in Fig. 2 for the m/z range 750–2500 of this PI sample. The mass spectra of slices taken through the dataset of the higher order aggregates are displayed to the left (Fig. 2I). Slice 2, Fig. 2I.E, corresponds to a series having $[PI_n+z\ cat]^{z+}$, $z = 2$ and $n = 2$–4. The resolved most abundant signals of +2 charge-state show a difference of 11.5 in m/z indicating that these mass differences relate to different degrees of sodium adduction. Slice 3, Fig. 2I.D, displays a series with $z = 3$ and $n = 4$–8 with 4 being least abundant, presence best viewed in Fig. 1A at $t_d(m/z)$ of ~42 (1250), and 5 most abundant. Similarly, slice 4, Fig. 2I.C, includes a series with $z = 4$ and $n = 8$, and so on. That is, we have resolved aggregated lipid ions into individual charge states, previously achieved for synthetic polymers up to charge-state families +23 [39,46].

The inset spectra of the total mass spectrum and slices through the dataset of the dimer and the monomer are displayed to the right in Fig. 2. Charge-state distribution $[(PI)_2+2cat]^{2+}$ and $[PI+cat]^+$ are resolved in t_d however not in m/z (isobars), making unequivocal assignments of the total mass spectrum (Fig. 2II.A) impossible. However, taking mass spectra of slices 1 and 2, corresponding to charge-state +1 and +2, respectively, unravels the charge-state convolution by making the low abundant feature of charge-state +1 now observable. Narrowing the area used for integration to obtain slices (here, Fig. 1B.3 Slice 1 left vs. right side) deconvolutes complexity for charge-state +1 further permitting differentiation between different charge carriers, e.g., H^+, NH_4^+, and Na^+ ionization, as is shown in Fig. II.D and II.E. Assignments of chain lengths and even degrees of unsaturation can now be obtained. We expect that decongestion of lipid complexity can be increased by narrowing the

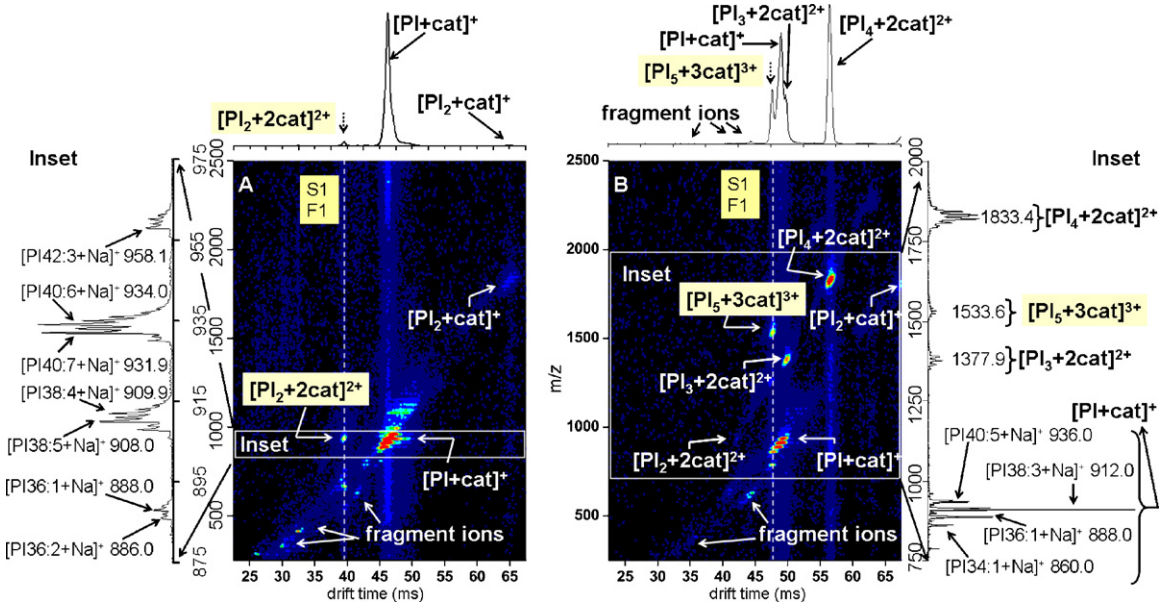

Fig. 3. Selection and activation studies of different phosphatidylinositol (PI) complexes. The dotted lines in the images indicate the drift time selections of (A) $[PI_2+2cat]^{2+}$ and (B) $[PI_5+3cat]^{3+}$. The t_d distribution (on top) and the mass spectra (left and right) provide details of the dissociated products. For any m/z, multiple compositions exist within the PI structure. For example, in (A), the ion labeled 931.9 is denoted as $[PI\ 40{:}7+Na]^+$. This ion could also be $[PI\ 38{:}4 - H+2\ Na]^+$ $[PI\ 42{:}4+H]^+$, for example. Similarly, the assignments of the singly charged ions in (B) are tentatively, e.g. $[PI36{:}1+Na]^+$ and $[PI38{:}4+H]^+$ ions are isobaric with the m/z value of 888.0. More details to the principle of selection and fragmentation of complexes are included in the Supplemental data. The assignments of the singly charged ions are tentatively, e.g., $[PI36{:}1+Na]^+$ and $[PI38{:}4+H]^+$ ions are isobaric with the m/z value of 888.0. More details to the principle of selection and fragmentation of complexes are included in the Supplemental data.

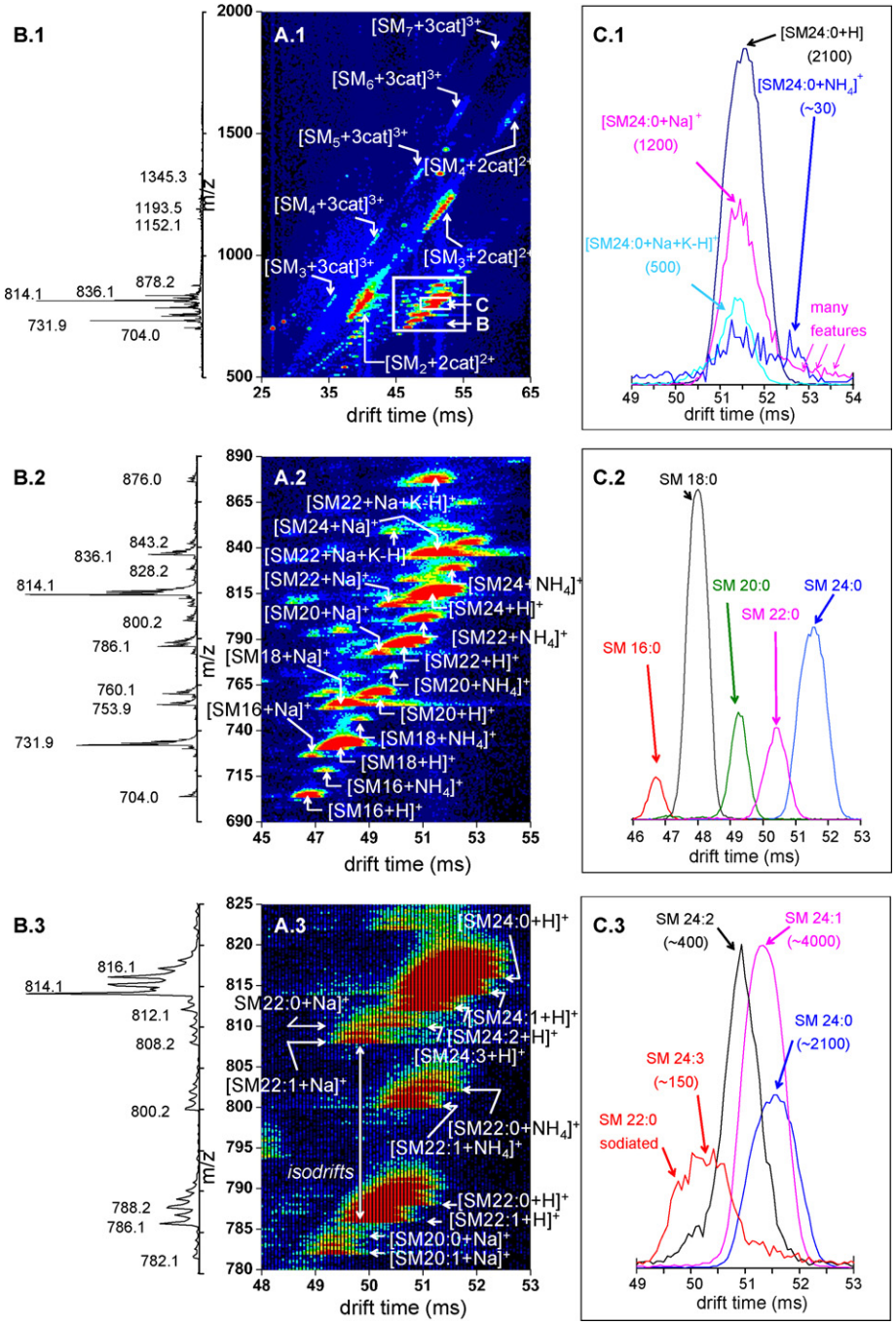

Fig. 4. Images, diagonally extracted mass spectra (slices), and drift time distributions of sphingomyelins (SM). (A.1) Full range: many different charge-state aggregates. (A.2) Inset of singly charged ions shows significant separation of about 5 ms between $[SM16+H]^+$ and $[SM24+H]^+$. Multiple different cations for each chain length populate the image; $[SM22+Na+K-H]^+$ and $[SM24+Na+K-H]^+$ are tentatively assigned as the m/z values could also be oxidized $[SM22_{ox}+2Na-H]^+$ and $[SM24_{ox}+2Na-H]^+$, however, one would expect a significant change in structure and cross section upon oxidation. (A.3) Inset of singly charged ions focusing on $[SM24+H]^+$ reveal that the slightly faster t_d features relate to an increasing degree in double bonds. This visualization makes it possible to determine that $[SM24:0+H]^+$ through $[SM24:3+H]^+$ are present. (B) Mass spectra of diagonal slices of $[SM+cat]^+$ in the respective mass range. (C) The t_d distributions; the numbers in brackets give the ion abundances when displayed on a different scale on the y-axis. (C.1) different ionizations of SM24:0. (C.2) different chain lengths of SM (results for protonated ions are displayed). (C.3) Different unsaturations of SM (results for protonated ions are displayed). The different charge carriers have little influence on this lipid structure as isodrifts are observed for all ions. The t_d distributions provide Δ values, on average, of about 1.2 ms for each ethylene increase in chain length and 0.3 ms for each unsaturation.

width of the diagonal slices even further as will be discussed for the analysis of sphingomyelin (SM) mixtures. The analysis of PI using slices through the dataset provides detailed information about the size distributions of the monomers as well as complexes existing over a wide range of charge states and sizes (i.e., $[PI_n+z\,cat]^{z+}$, where z ranges from 1 to 6 and n from 1 to 16).

The minimum size limits for each charge-state >+2 are $[PI_4+3cat]^{3+}$, $[PI_8+4cat]^{4+}$, $[PI_{11}+5cat]^{5+}$, and $[PI_{16}+6cat]^{6+}$. The lipid to charge ratio (n/z) in lipid aggregates changes significantly from 4:3 (1.3) to 16:6 (2.6). There is indication that the maximum size limit for each charge-state is larger than the mass range these experiments were performed. For example, charge states with $z=5$ and 6 show resolved signals at $m/z \sim 1790$–1850 (Fig. 2I.A and I.B) with mass differences of about 24 Da corresponding to one ethylene unit. We tentatively assign these to the principle composition $[M_2+cat]^+$ of dissociated products from higher order structures.

Examination of the total t_d distributions displayed above the IMS-MS datasets in Fig. 1 shows charge-state families and their abundances. The most abundant charge-state is $[(PI)_2+2cat]^{2+}$ at about 40 ms followed by $[(PI)_5+3cat]^{3+}$ at about 48 ms as well as $[(PI)_3+2cat]^{2+}$ at about 51 ms. The mass spectrum of the higher order aggregates (Fig. 1B.2, bottom left) reveals that the most abundant complexes have an even number of charges. For example, the intensities for charge-state $[PI_9+4cat]^{4+}$ and $[PI_{10}+4cat]^{4+}$ are higher than for $[PI_7+3cat]^{3+}$ and $[PI_{12}+5cat]^{5+}$ as well as $[PI_{13}+5cat]^{5+}$ and $[PI_8+3cat]^{3+}$, respectively. This is in accordance with the intense ion abundances of the doubly charged dimer $[PI_2+2cat]^{2+}$ vs. the low-abundant monomer $[PI+cat]^+$ drift time distribution (Fig. 1, top left).

It is interesting to examine the behavior of these ions under the influence of additional energy. Dissociation experiments using 220 V, the voltage usually applied for fragment ion analysis, on PI complex $[(PI)_2+2cat]^{2+}$ (Fig. 3A) displays results after activation, an IMS2-MS experiment, performed by t_d selection and dissociation, produced $[PI+cat]^+$ along with little fragmentation of the lipid. Higher order aggregates $[(PI)_5+3cat]^{3+}$ (Fig. 3B) produced intricate patterns of dissociated products that include $[(PI)_2+2cat]^{2+}$, $[(PI)_3+2cat]^{2+}$, $[(PI)_4+2cat]^{2+}$, $[PI+cat]^+$ (the latter two are the most abundant features), and $[(PI)_2+cat]^+$. In an IMS^3-MS experiment, selection and activation of the higher order aggregate $[(PI)_3+2cat]^{2+}$ produced $[PI+cat]^+$ along with increasing fragmentation of covalent bonds. In all these dissociation experiments, under conditions that commonly introduce covalent bond cleavages, we still observe intact aggregates that did not dissociate into smaller aggregate units or their monomer. The successful dissociation of the higher order aggregates $[PI_2+2\ cat]^{2+}$ and $[PI_5+3\ cat]^{3+}$ allows us to assign the molecular makeup of each inverted micelle as shown by the resolved signals in the Inset spectra in Fig. 3 displaying the dissociated monomers.

Some tendency for aggregation is observed for many different smaller and structurally simpler lipids such as the *N*-acyl amino acids and monoglycerides using an IMS-MS approach [48,49]. For example, *N*-oleoyl glycine (OLGly) produced $[(OlGly)_n+cat]^+$ with $n = 2–3$ aggregates. Endocannabinoid *N*-arachidonoyl ethanolamide (anandamide, AEA) showed the ability to form $[(AEA)_n+z\ cat]^{z+}$ with $z = 1$ and $n = 2–3$ as well as $z = 2$ and $n = 3–8$, respectively. Higher order aggregates of charge states >2 are not observed. The aggregates ≤ 2 are also rather labile as some dissociate as metastable complexes. Activation experiments (220 V) effectively dissociate these lipid complexes into monomer units as well as produce a considerable degree of fragment ions related to covalent bond cleavages.

Other phospholipids such as sphingomyelins (SM, Fig. 4A.1), phospatidylcholins (PC, Fig. 6C), phosphatidylglycerol (PG, Fig. 7A), phosphatidylethanolamine (PE) with up to $[PE_9+3cat]^{3+}$ all showed significant tendencies for the formation of aggregates. Aggregation is somewhat reduced by diluting the sample concentration in solution. For example, diluting the PI sample by a factor of 100 reduced the highest charge-state aggregation from +6 to +4.

Accumulative results indicate that the higher order aggregates are associated with phospholipids. As described for PI in greater detail, phospholipid aggregates (Fig. 3) are considerably more stable than the aggregates of simpler lipids [48,49]. We attribute the extreme tendency and stability of the phospholipids for the formation of aggregates in the form of inverted micelles to the presence of both positive and negative charges on the lipid head groups interacting and forming the core by salt bridges while the fatty acid chains provide the hydrophobic shell exposed to the hydrophobic gas-phase environment.

Micelles are receiving increasing attention recently [50–52]. Phospholipid work reported on the existence of dimers $[M_2+cat]^+$ utilizing a range of different ionization techniques including MALDI and ESI coupled to mass spectrometers [53, and citations therein]; signals that appear to relate to higher order aggregates are commonly not assigned in these mass spectra. This interesting behavior is in contrast to other biological molecules such as peptides that are commonly observed as $[M_n+z\ cat]^{z+}$ with $n = 1–2$ in ESI-MS. The micelle formation affects sensitivity, quantitation, as well as data interpretation in MS of (phospho) lipids without the use of IMS. The overlaps of different ionizations (H^+, Na^+, $NH4^+$ etc.) of charge-state +1 are readily assigned that contribute to the mass spectral complexity and difficulties in unequivocal assignments of differences due to ionization, chain length, and unsaturation. The results of the total mass spectra indicate the limitations of MS alone, especially for quantitative results, as many features are not observed or interpretable. IMS-MS provides a detailed pictorial and molecular makeup from the entire sample that is ionized.

3.2. General trends associated with chain length, unsaturation, and ionization

Fig. 4 shows the two-dimensional dataset for sphingomyelins measured in transmission mode. The majority of signals associated with sphingomyelins relate, again, to aggregation with charge states +1 to +3 (Fig. 4A.1). These aggregates, especially the higher charge states, are not very noticeable in the total mass spectrum (Fig. 4B.1) because of the low signal-to-noise ratio as compared to the higher abundant, frequently isobaric charge states such as $[SM_2+2cat]^{2+}$ and $[SM+cat]^+$. Because of the exquisite sensitivity for the entire sample composition, the IMS approach makes these ions observable. Additionally, the convolution of charge states, for example $[SM_3+3cat]^{3+}$, $[SM_2+2cat]^{2+}$, and $[SM+cat]^+$, makes each of the micelles possible to examine with the incorporation of IMS. Diagonally extracted slices through the two-dimensional dataset give mass spectra that deconvolute complexity observed with the different charges states, as exemplified by the mass spectra shown in Fig. 4B.2 and B.3. The analysis of extracted slices from the two-dimensional dataset permits examining in detail the different charge-state distributions even of low-abundant ions of charge-state + 3 aggregates that would otherwise be convoluted, e.g., $[SM_3+3cat]^{3+}$ with isobaric, higher abundant charge states $[SM_2+2cat]^{2+}$ and $[SM+cat]^+$ (Fig. 4A.1).

It is appealing to examine regions of this dataset over narrower ranges. Fig. 4A.2 shows an inset of the region $t_d(m/z)$ 45(690)–55(890) and Fig. 4A.3 an inset of the region $t_d(m/z)$ 48(780)–53(825). Clearly, ESI-IMS-MS provides an abundance of data that produces intricate but regular patterns when examining inset regions. Inspection of the insets reveals that separation between chain length (Fig. 4A.2) and unsaturation (Fig. 4A.3) is achieved. The inset of singly charged ions focusing on the $t_d(m/z)$ region of $[SM24+H]^+$ provides an interesting display of features that not only differ by two mass units but is readily distinguished visually. These slightly different features relate to double bonds that, with increasing unsaturation, drift faster through the drift gas revealing the presence of more compact structures. This visualization makes it possible to determine that $[SM24:3+H]^+$ is present along with $[SM24:0+H]^+$ through $[SM24:2+H]^+$ which would otherwise be incorrectly assigned to $[SM22:0+Na]^+$ only. From the pictorial, different ionizations are observed at about the same t_d's for saturated and unsaturated SM ions (H^+, Na^+, and mixed ionization), respectively, with the exception of additional abundant features for NH_4^+.

Extractions of t_d distributions provide exact t_d values of the abundant feature for a given m/z (Fig. 4C) and give insight to the high-efficiency separation. The most abundant features for differently ionized SM24:0 molecules (Fig. 4C.1) such as adduction of H^+, Na^+, NH_4^+ or mixed ionization of Na^+ and K^+ have the same t_d (isodrifts). The result of the isodrifts at ~51.6 ms reveals that the cations

have little influence on the cross section of these ions. This indicates that the polar head group interacting with the charge is not significantly altered by the cation size and the fatty acid backbone of the SM lipid is structurally not crucial in forming the gas-phase conformation. The fatty acid moiety is likely not interacting strongly with the charge so that the cation type does not alter its configuration. However, the cations have different sizes so either the size difference is not sufficient to change the cross section significantly or the polar head group is reduced in size to compensate for the larger cations. It is conceivable that the proton is being bound to a single site whereas NH_4^+ and Na^+ are sufficiently large to complex with more than one site, thus shrinking or expanding the head group.

A closer view shows that NH_4^+ has an additional abundance at ~1.2 ms slower indicating that there is a stable, possibly more open, structure that differs from the conformation of the other ionizations. Low-abundant features additional to the high abundant isodrifts are also observed for Na^+ ionization between $t_d \sim 52.4$ and ~55 ms.

Examining the ionization behavior of 1-palmitoyl-2-oleoyl-sn-glycerol (1-pal-2-ol glycerol), a lipid with a glycerol instead of a ceramide based core, shows a similar trend (Supplemental). Again, $[M+cat]^+$ with cat = H^+, NH_4^+ and Na^+ are detected as isodrifts, here at ~42.5 ms. Low-abundant features are also observed for both sodiated and ammonium adducted 1-pal-2-ol glycerol extending to ~50 ms.

The behavior of lipid ions is in contrast to other biological molecules such as peptides as well as synthetic polymers in which different cations frequently influence the structure of the molecule noticeably [39,54,55]. However, bradykinin also showed similar drift times with different cations attached in a temperature range from 300 to 600 K [56].

On the other hand, lipids differing only by an ethylene in the hydrocarbon tail are baseline separated with t_d differences of, on average, ~1.2 ms as is shown for the protonated fully saturated SM ions (Fig. 4C.2). As one would expect with decreasing chain lengths the ions travel faster. Different unsaturations (Fig. 4C.3) are partially separated with t_d differences of, on average, ~0.3 ms as displayed for the protonated SM ions. With increasing unsaturation the ions travel faster indicating a more compact structure. We can conclude that lipid ions reveal different structures that can be exploited for gas-phase separation. IMS-MS efficiently separates SM ions in the gas-phase based on their charge states, e.g., $[SM+cat]^+$ through $[SM_3+3cat]^{3+}$, and shapes, e.g., $[SM16+H]^+$ through $[SM24+H]^+$ and $[SM24:0+H]^+$ through $[SM24:3+H]^+$, prior to mass spectrometric analysis.

Of interest is also the gas-phase separation efficiency for different phospholipids afforded by IMS. Fig. 5 provides an overview of the results focusing on the singly charged ions displayed by an identical inset range of $t_d(m/z)$ values between 44(700) and 54(850). ESI generated ions from each phospholipid mixture containing different *N*-acyl lengths as well as different ionizations display distinctive images. Small changes in the mass of the lipid ions, brought about by head group differences are readily resolved by IMS-MS even when t_d differences are small. As an example, the difference in drift time separation of PE, PC, and PG are on average ~0.6 ms. The usefulness of the two-dimensionality of the IMS-MS approach becomes evident in this comparison. The m/z values of the two different lipids and ionizations are sufficiently different so that these individual ions occupy different $t_d(m/z)$ areas. For detailed analysis, mass spectra for each lipid can be obtained by extracting m/z values diagonally through the dataset: in this case, through the features 24 mass units apart (one ethylene unit), as seen in Figs. 2 and 4B for PI and SM, respectively. The drift time separation of the different phospholipids is PE < PC < PG < SM (Fig. 5). As expected, lipids with the same glycerol core separate according to size requirements of the head group. For example, the ethanolamine (Fig. 5A) is smaller than the glycerol (Fig. 5C) and travels consequently faster through the drift gas.

The comparison between different phospholipid classes was recently reported using MALDI-IMS-MS [40]. In our ESI-IMS-MS work, features of SM and PC mixtures (Scheme 1) are cleanly separated by this solvent-free gas phase separation approach (compare dotted line in Fig. 5B and D). For example, the same choline head group reveals differences between PC, longest t_d at ~48.9(789.1), and SM, longest t_d at ~51.2(790.3), of ~2.3 ms (Fig. 5B and D). Thus, the ceramide core of SM provides longer drift times and thus larger collision cross sections as compared to the glycerol core of PC. Interestingly, SM shows notably longer drift times as compared to any phospholipid with a glycerol core and similar size aspects of the head group (Fig. 5A–C). SM reveals shorter drift times than PI with longest t_d at ~52.0(934.0) (Fig. 1B.3) carrying a larger polar head group. The ceramide core with its double bond must have a significant structural influence, perhaps best described by a kink caused by the double bond, opening up the SM conformation. The largest separation between all phospholipids, however, is observed for the PI mixture (Fig. 1B.3, singly charged ions) occupying the inset area of ~47(860) and ~52(970), a significant shift caused by the additional mass and size of the inositol head group.

The experimental values of $t_d(m/z)$ are sufficiently different for the different polar head groups to provide efficient separation. This indicates that many lipid molecules could be identified based on $t_d(m/z)$ values. Phospholipid analysis is classically achieved by reversed phase LC that separates according to length and saturation of *N*-acyl chains or normal phase LC according to primarily the head group prior to MS and MS/MS detection [57,58]. IMS-MS provides simplicity (no solvents or columns) and time-savings (no trouble shooting or sample loss to the column). Perhaps most importantly, the high sensitivity to the entire sample composition along with the respective pictorial display makes this technology ideal for comparative analysis of samples especially important for relative quantitative assessments; in analogy similar to 2D gels for protein analysis.

3.3. General trends associated with ion suppression and ionization

Here, by examining the usefulness of ESI-IMS-MS for the analysis of low-abundant lipids in complex mixtures, we address issues related to ion suppression in complex mixtures that hamper global lipidomics analysis. Ionization-suppressed *N*-palmitoyl glycine (PALGly) was mixed in high concentration (5.8 mM), in the presence of AEA in the lowest concentration (116 μM) and readily ionized PC in high concentration (8.7 mM) making a molar ratio of 50:1:75. This mixture was used for concentration studies ranging from 10,000:1 to 1:1 without prior sample cleanup or optimization procedures. Fig. 6 displays the result for three different mixture dilutions, 10,000:1, 100:1, and 1:1, corresponding to (A) 580 nM, (B) 58 μM, and (C) 5.8 mM PALGly, respectively, in each mixture.

The IMS-MS images allow ready visualization of significant changes in the mixtures. PALGly, a negative lipid, was detected in 580 nM concentration (Fig. 6A) in positive ion mode. With increasing concentrations the signal intensities for AEA and PC increase drastically, as does the chemical noise (Fig. 6B), and the aggregation (Fig. 6B and C), mainly caused by PC. $[(PALGly)_2+cat]^+$ is present in Fig. 6B but not in 6.C. For more details, total mass spectra were extracted for each lipid mixture concentration and overlaid (Fig. 6D–F).

The mass spectra provide a better appreciation of changes in ion abundances than do the images. The low overall intensity of PALGly, as seen in the overlaid insets of the total mass spectra (Fig. 6E), is affected by the detection of $[M+Na]^+$ in addition to $[M+H]^+$ and by

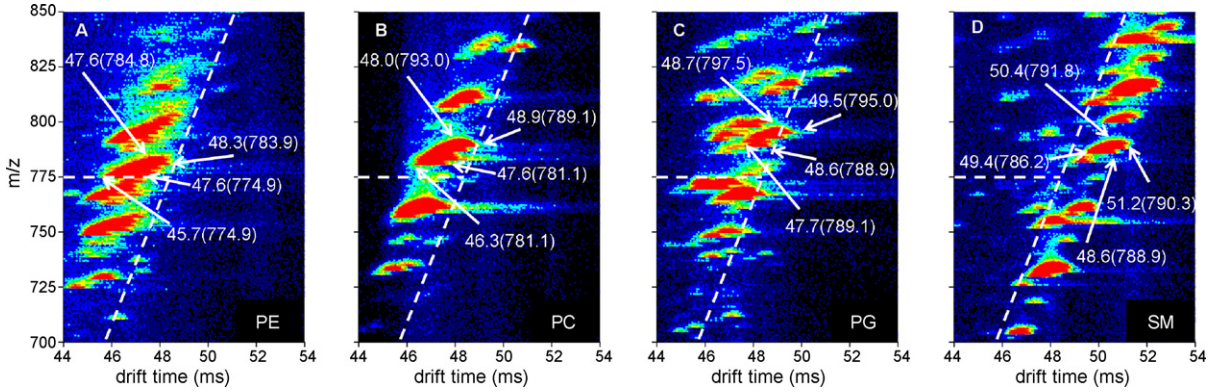

Fig. 5. Insets of images displaying the singly charged ions of phospholipids (A) PE, (B) PC, (C) PG, and (D) SM with their respective $t_d(m/z)$ values of features with similar m/z 775–795. Two white lines are included to guide the eye for changes within (A) through (D), respectively. All phospholipids are separated according to $t_d(m/z)$ values. Also note the separation of PI sample (Fig. 1B.3).

aggregation $[(PALGly)_2+cat]^+ = H^+$ and Na^+ (Fig. 6D). As expected, low ion abundance of PALGly, a negative lipid, is caused by the ion suppression imposed by the positively charged PC phospholipid (Fig. 6F) present at similar concentrations as PALGly as well as the easily ionized AEA, in form of $[AEA+cat]^+$ and $[(AEA)_2+cat]^+$ with cat = H^+ and Na^+ (Fig. 6D), at 50-fold lower concentration. The ion abundance of $[PALGly+cat]^+$ with cat = H^+ and Na^+ (Fig. 6E) increases for the 100:1 (ion abundances 151, 223) relative to the 10,000:1 dilution (ion abundances 39, 52) but decreases at the highest concentration in the 1:1 dilution. Additionally, only the protonated ion (ion abundance 71) is detected in the highest concentration and not the sodiated PALGly. Interestingly, the ion abundance for the protonated PALGly in all concentrations is less affected than the sodiated ion. Taking all these observations into account, we conclude that the inability to detect the PALGly, particularly the sodiated ion, indicates that this lipid is incorporated into the PC micelles.

By comparison with the drastically increasing ion abundance in the mass spectral signal of protonated PC with increasing concen-

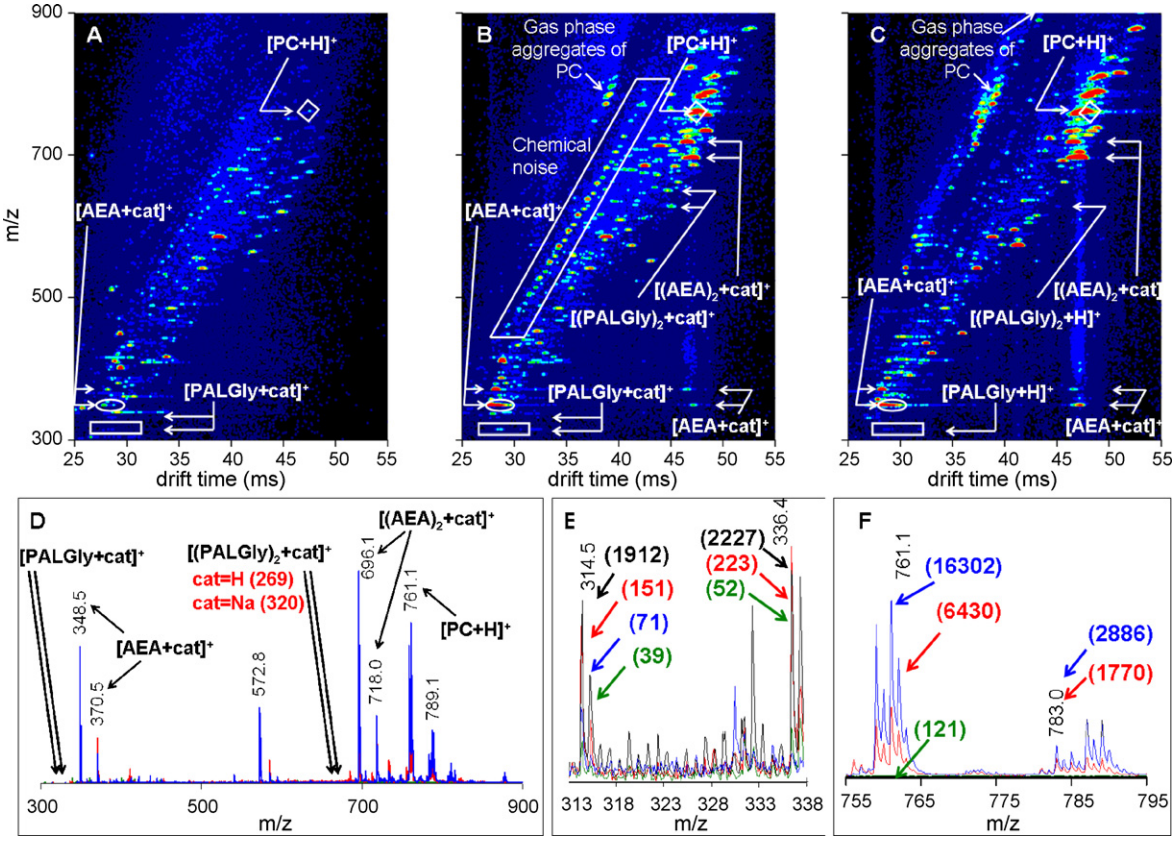

Fig. 6. Analysis of mixtures of chemically extremely different lipids, *N*-palmitoyl glycine (PALGly, 5.8 mM), *N*-arachidonoyl ethanolamide (AEA, 116 μM) and phosphatidylcholine (PC, 8.7 mM), that represent general classes relevant to the biosynthesis of endocannabinoid-like lipids. This set of experiments examines the ability to analyze ionization-retarded PALGly, a negative lipid, using positive ionization and dependent on different overall lipid mixture concentrations. Images of (A) 10,000:1; (B) 100:1; (C) 1:1 in the mixture dilutions. The comparison of the images provides a visualization of the changes. Notably in (B) The chemical noise is significantly increased. (C) Shows evidence for gas-phase aggregation similar to the pure samples (data not shown). Total mass spectra for the three mixture concentrations are 10,000:1 (green), 100:1 (red), 1:1 (blue) and the values in brackets provide the ion abundance for each signal in the respective inset display: (D) All mixture components, (E) PALGly (pure compound is in black), and (F) PC. Signal intensities of AEA and PC increase with concentrations, however, the abundance for PALGly barely changes, in fact, a change in concentration of 10,000 shows about the same intensities (39 vs. 71). In the highest concentration PALGly is not detected with any appreciable intensity.

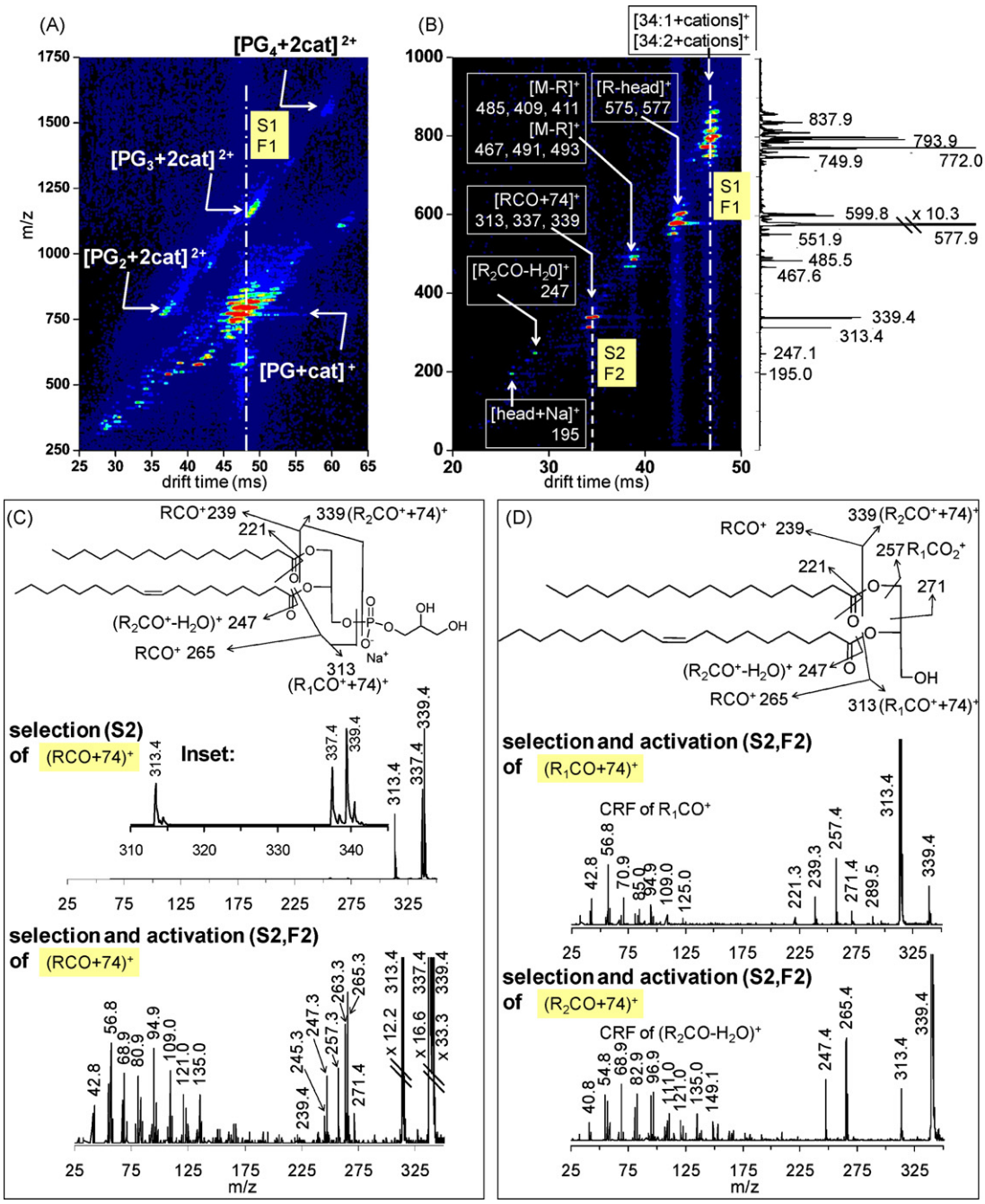

Fig. 7. Multidimensional IMS^3-MS analysis for detailed characterization of complex mixtures of closely related molecules of phosphatidylglycerols (PG). (A) IMS-MS image indicating where t_d precursor ions of 47.2 ms (width 0.2 ms) will be selected (S1) at G2 and fragmented (F1) with 220 V at IA2. (B) IMS^2-MS image: the fragment ions produced are separated from each other. Similar fragment ions appear at similar t_d's, e.g., $[RCO]^+$ with signals m/z 313, m/z 337, and m/z 339. We selected (S2) and fragmented (F2) in the middle of the $[RCO]^+$ fragment family to attain IMS^3-MS of all three $[RCO]^+$ fragment ions alike. (C) Extracted total mass spectra from selection as well as from selection and activation experiments for IMS^3-MS studies of $[RCO]^+$ family of PG. (D) Extracted total mass spectra from IMS^3-MS experiments of $[R_1CO]^+$ and $[R_2CO]^+$ of 1-palmitoyl-2-oleoyl-glycerol after careful selections between very closely related fragment ion structures. Results from (D) are used to exemplify results obtained in (C) for structure elucidation of *sn*-1 and *sn*-2 of isomeric compositions.

tration (Fig. 6F; ion abundances 121 < 6430 < 16,302 for $[PC+H]^+$), it is evident that the ion abundance of PALGly changes very little over a 10,000–fold concentration range (Fig. 6E). For the 1:10,000 dilution, pure PALGly (350 nM) was readily detected with an ion abundance of 1912 for the protonated ion and 2227 for the sodiated ion while PALGly in the mixture (580 nM) gave a signal with an ion abundance of 39 only for the protonated ion (Fig. 6E, data displayed in black). As expected, we observe a large signal decrease in the mixture relative to the pure compound for the detection of the ionization suppressed PALGly. The decongestion of sample complexity achieved by incorporating IMS permits reliable detection of ionization-retarded compounds.

As shown here, IMS-MS integrates high-efficiency solvent-free gas-phase separation to MS resulting in more comprehensive detection of all sample components. Even if PALGly would be detected in such a complex mixture by MS without the incorporation of IMS, tandem MS studies necessary for structural elucidation would be problematic because of the low ion abundance (Fig. 6D). Low-abundant lipid molecules can be identified based on values of m/z and t_d provided by IMS-MS without the need for fragmentation

analysis [48,49]. As shown here, IMS-MS has a pictorial means to compare different samples quickly, e.g., the presence of the phospholipids is unraveled by the intense presence of aggregates. Most important in this context is that we can reliably analyze the biological significant class of *N*-acyl amino acids, here PAL-Gly, in the presence of two possible lipid precursor classes, AEA and phospholipids [2,5,10,11]. This progress in lipid identification is stimulating as it highlights the usefulness of IMS for decongestion of lipid complexity without prior solvent-based separation approaches indicating applicability for tissue imaging of signaling lipids by mass spectrometry.

3.4. Multidimensional IMS-MS for structural elucidation by fragment ion analysis

Multidimensional IMS-MS analyses of phospholipids lead to a wealth of information. Drift time selection of a precursor ion also embraces any ion within this particular drift time window. The selection of t_d 48.1 ms of the SM sample provided two abundant species corresponding to $[SM18:0+H]^+$ and $[SM18:0+Na]^+$ (isodrifts). Subsequent activation by applying energy of 200 V produced fragment ions at m/z 184 corresponding to the loss of the choline head group, along with a less abundant signal at m/z 125. The selection of t_d 46.5 ms of the PC sample produced fragment ions identical to the SM study. This IMS^2-MS result reproduces MS^2 achievements from early work on PC [59].

IMS^3-MS was employed for the structural elucidation of a phosphatidylglycerol (PG) mixture (Fig. 7). The results of the IMS-MS experiment along with the respective selection and activation (dotted line; S1 F1) for the subsequent IMS^2-MS experiment is shown in Fig. 7A. Instrumentally, the selection at G2 of t_d 47.2 ms provides the drift-selected precursor ions of PG34:1 and PG34:2 both in protonated and sodiated form (isodrifts). These drift-time selected ions when exposed to elevated voltage, here 220 V at IA2, in the middle of the drift tube provide numerous abundant fragment ions. As can be seen in the 3D display for the result of this IMS^2-MS experiment (Fig. 7B), the fragment ions are separated in the rest of the drift tube as fragment ion sets from each other as well as from the precursor ions. For example, the fragment ions of $[RCO+74]^+$ with m/z 313, 337, and 339 at $\sim t_d$ 34.5 ms are drift separated from $[M-R]^+$ with m/z 485, 409, 411, 467, 491, and 493 at $\sim t_d$ 38.6 ms. Thus, the separation of the fragment ions according to size, shape, and charge produce unique groupings of certain types of fragment ions as is shown in Fig. 7B. This separation then permits the t_d selection at G3 of any fragment ion of interest to provide IMS^3-MS analysis by drift-selecting fragment precursor ions that are activated at IA3 for further fragmentation. Tedious selection was not applied to the PG mixture. Instead, as one can see in the pictorial display in Fig. 7B, ions were selected through the middle of the respective fragment ion grouping. For example, the $[RCO+74]^+$ fragment ion family were t_d selected and fragmented (dotted line S2 F2) to obtain IMS^3-MS of all three $[RCO+74]^+$ fragment ions. Results for such an IMS^3-MS analysis are shown in Fig. 7C for the $[RCO+74]^+$ group, displaying the total mass spectrum.

The total mass spectra of the selection and activation experiment for the IMS^3 analysis of the PG mixture (Fig. 7C) are compared with those of IMS^3-MS results obtained by carefully selected drift times for 1-palmitoyl-2-oleoyl-glycerol (Fig. 7D). The assignments of the structural positions of the PG mixture are straightforward: m/z 239 and 257 relate to *sn*-1, whereas m/z 245 and 247 with $[RCO\text{-}H_2O]^+$ as well as m/z 263 and 265 correspond to *sn*-2. The assignments of the fragment ion structures such as $[RCO-H_2O]^+$ are according to previous work on these system [60]. Fragment ions with $m/z < 150$ correspond to charge-remote fragmentation [16,17]. The results reveal that ESI-IMS^3-MS tandem fragment ion analysis distinguishes between *sn*-1 and *sn*-2 positions of glyceride moieties in that the composition of the drift-selected precursor ions is *sn*-1 16:0 and *sn*-2 18:1 for PG 34:1 as well as *sn*-1 16:0 and *sn*-2 18:2 for PG 34:2. The other theoretical composition of *sn*-1 16:1 and *sn*-2 18:1 for PG 34:2 is not present in the selection at 47.2 ms. Structural elucidation of *sn*-1 and *sn*-2 positions utilizing tandem MS examinations are frequently based on as little as abundance ratios [61]. Here, we show that we can obtain detailed structural analysis of all lipid components even of isomeric composition and that multidimensional IMS-MS analysis adds the additional dimension of size, shape, and charge based separation to fragment ion analysis.

4. Conclusions

Multidimensional IMS-MS is shown to reduce the complexity of lipid mixtures, including those of acidic, neutral, and basic lipids, and provides considerable detail relating to their structural composition. IMS-MS analysis makes it possible to observe a range of low-abundance lipids that would normally be lost in the background if only MS is used for the analysis. Perhaps most important here is the snapshot of sample composition with an extreme wealth of extractable data for qualitative (m/z) and quantitative (t_d abundance) assessment of molecular makeup of the entire ionized sample composition intrinsically always examined under identical separation and MS conditions. Also observed are families of isomeric species that are readily discerned by multidimensional IMS^3-MS. However, to gain improved efficacy in sample complexity, ionization methods are required that, ideally, ionize all neutral, negative, and positive lipids alike, as expected to be present in biosynthetic pathways [2,5,10,11,34–37], aiding improved sensitivity and scrutiny of the entire sample as has been examined for biological [17,62,63] and synthetic systems even when insoluble [64–66]. The high-efficiency separation introduced by IMS-MS technology holds promise to determine sample composition for which LC separation is not optional such as in tissue imaging mass spectrometry [67]. Future work will address why lipids ionized with different cations frequently produce isodrifts, ions in which the charge carriers have little to no structural influence, as well as detailed views on inverted micelle structure and composition.

Acknowledgments

The authors are grateful for having been inspired by Prof. J. Michael Walker (1950-2008), a gifted mentor, kind colleague, and friend. The authors are thankful for the support of grants from the National Institutes of Health/National Institute on Drug Abuse (DA16825, DA018224), the Linda and Jack Gill Center for Biomolecular Science, Indiana University, and the MetaCyt Grant to Indiana University from the Lilly Foundation Inc., Indianapolis IN. We thank Dr. Susan M. Huang (Johns Hopkins University) for critical comments and suggestions to this work.

Appendix A. Supplementary data

Supplementary data associated with this article can be found, in the online version, at doi:10.1016/j.ijms.2008.12.020.

References

[1] J.M. Walker, S.M. Huang, N.M. Strangman, K. Tsou, M.C. Sanudo-Pena, Proceedings of the National Academy of Sciences of the United States of America, vol. 96, 1999, p. 12198.
[2] S.M. Huang, T. Bisogno, T.J. Petros, S.Y. Chang, P.A. Zavitsanos, R.E. Zipkin, R. Sivakumar, A. Coop, D.Y. Maeda, L. De Petrocellis, S. Burstein, V. Di Marzo, J.M. Walker, J. Biol. Chem. 276 (2001) 42639.
[3] S.M. Huang, T. Bisogno, M. Trevisani, A. Al-Hayani, L. De Petrocellis, F. Fezza, M. Tognetto, T.J. Petros, J.F. Krey, C.J. Chu, J.D. Miller, S.N. Davies, P. Geppetti, J.M. Walker, V. Di Marzo, Proceedings of the National Academy of Sciences of the United States of America, vol. 99, 2002, p. 8400.

[4] J.M. Walker, S.M. Huang, Pharmacol. Ther. 95 (2002) 127.
[5] J.M. Walker, J.F. Krey, J.S. Chen, E. Vefring, J.A. Jahnsen, H. Bradshaw, S.M. Huang, Prostag. Oth. Lipid M. 77 (2005) 35.
[6] S.M. Huang, J.M. Walker, J. Neurophysiol. 95 (2006) 1207.
[7] B. Tan, H.B. Bradshaw, N. Rimmerman, H. Srinivasan, Y.W. Yu, J.F. Krey, M.F. Monn, J.S.C. Chen, S.S.J. Hu, S.R. Pickens, J.M. Walker, AAPS J. 8 (2006) E461.
[8] S.S.J. Hu, H.B. Bradshaw, J.S.C. Chen, B. Tan, J.M. Walker, Br. J. Pharmacol. 153 (2008) 1538.
[9] N. Rimmerman, H.B. Bradshaw, H.V. Hughes, J.S.-C. Chen, S.S.-J. Hu, D. McHugh, E. Vefring, J.A. Jahnsen, E.L. Thompson, K. Masuda, B.F. Cravatt, S. Burstein, M.R. Vasko, A.L. Prieto, J.M. Walker, Mol. Pharmacol. 74 (2008) 213.
[10] B. Tan, D.K. O'Dell, Y.W. Yu, M.F. Monn, H.V. Hughes, S. Burstein, J.M. Walker, Identification of endogenous N-acyl amino acids based on targeted lipidomics, J. Lipid Res. under revision.
[11] B. Tan, Y.W. Yu, M.F. Monn, H.V. Hughes, D.K. O'Dell, J.M. Walker, Targeted approach for identification of endogenous N-acyl amino acids in rodent brain tissue, J. Chromatogr. B. in press.
[12] R.C. Murphy, K.A. Harrison, Mass Spectrom. Rev. 13 (1994) 57.
[13] X. Han, R.W. Gross, Mass Spectrom. Rev. 24 (2004) 367.
[14] F.F. Hsu, J. Turk, Modern Methods for Lipid Analysis by Liquid Chromatography/Mass Spectrometry and Related Techniques, 2005, p. 61.
[15] S.H. Lee, M.V. Williams, I.A. Blair, Prostag. Oth. Lipid M. 77 (2005) 141.
[16] F.F. Hsu, J. Turk, J. Am. Soc. Mass Spectrom. 11 (2000) 892.
[17] S. Trimpin, D.E. Clemmer, C.N. McEwen, J. Am. Soc. Mass Spectrom. 18 (2007) 1967.
[18] A.D. Postle, D.C. Wilton, A.N. Hunt, G.S. Attard, Prog. Lipid Res. 46 (2007) 200.
[19] A. Devakumar, D.K. O'Dell, J.M. Walker, J.P. Reilly, J. Am. Soc. Mass. Spectrom. 19 (2008) 14.
[20] R.C. Murphy, M. Fitzgerald, R.M. Barkley, Metab. Metab. Profiling (2008) 161.
[21] X. Han, R.W. Gross, Metab. Metab. Profiling (2008) 134.
[22] S. Trimpin, A.E. Mixon, M. Stapels, M.Y. Kim, P.S. Spencer, M.L. Deinzer, Biochemistry 43 (2004) 2091.
[23] M. Vogeser, G. Schelling, Clin. Chem. Lab Med. 45 (2007) 1023.
[24] J.T. Lin, A. Arcinas, J. Agric. Food Chem. 56 (2008) 4909.
[25] M.Y. Golovko, E.J. Murphy, J. Lipid Res. 49 (2008) 893.
[26] X. Han, Front. Biosci. 12 (2007) 2601.
[27] M.J. Wakelam, T.R. Pettitt, A.D. Postle, Meth. Enzymol. 432 (2007) 233.
[28] J. Gobey, M. Cole, J. Janiszewski, T. Covey, T. Chau, P. Kovarik, J. Corr, Anal. Chem. 77 (2005) 5643.
[29] G. Sun, K. Yang, Z. Zhao, S. Guan, X. Han, R.W. Gross, Anal. Chem. 79 (2007) 6629.
[30] J. Schiller, R. Suss, B. Fuchs, M. Muller, O. Zschornig, K. Arnold, Front. Biosci. 12 (2007) 2568.
[31] A.N. Krutchinsky, B.T. Chait, J. Am. Soc. Mass Spectrom. 13 (2002) 129.
[32] B.L. Peterson, B.S. Cummings, Biomed. Chromatogr. 20 (2006) 227.
[33] E.P. Go, J.V. Apon, G. Luo, A. Saghatelian, R.H. Daniels, V. Sahi, R. Dubrow, B.F. Cravatt, A. Vertes, G. Siuzdak, Anal. Chem. 77 (2005) 1641.
[34] V. Di Marzo, A. Fontana, H. Cadas, S. Schinelli, G. Cimino, J.C. Schwartz, D. Piomelli, Nature 372 (1994) 686.
[35] Y. Okamoto, J. Morishita, K. Tsuboi, T. Tonai, N. Ueda, J. Biol. Chem. 279 (2004) 5298.
[36] J.P. Slotte, B. Ramstedt, Eur. J. Lipid Sci. Technol. 109 (2007) 977.
[37] S.I. Rapoport, Prostag. Oth. Lipid M. 77 (2005) 185.
[38] X. Liu, S.J. Valentine, M.D. Plasencia, S. Trimpin, S. Naylor, D.E. Clemmer, J. Am. Soc. Mass. Spectrom. 18 (2007) 1249.
[39] S. Trimpin, D.E. Clemmer, Anal. Chem. 80 (2008) 9073–9083.
[40] S.N. Jackson, M. Ugarov, J.D. Post, T. Egan, D. Langlais, J.A. Schultz, A.S. Woods, J. Am. Soc. Mass Spectrom. 19 (2008) 1655–1662.
[41] A.B. Kanu, P. Dwivedi, M. Tam, L. Matz, H.H. Hill Jr., J. Mass Spectrom. 43 (2008) 1.
[42] B.C. Bohrer, S.I. Merenbloom, S.L. Koeniger, A.E. Hilderbrand, D.E. Clemmer, Annu. Rev. Anal. Chem. 1 (2008) 293.
[43] C.A. Srebalus, J.W. Li, W.S. Marshall, D.E. Clemmer, Anal. Chem. 71 (1999) 3918.
[44] S.L. Koeniger, S.I. Merenbloom, S.J. Valentine, M.F. Jarrold, H. Udseth, R. Smith, D.E. Clemmer, Anal. Chem. 78 (2006) 4161.
[45] S.I. Merenbloom, S.L. Koeniger, S.J. Valentine, M.D. Plasencia, D.E. Clemmer, Anal. Chem. 78 (2006) 2802.
[46] S. Trimpin, M.L. Plasencia, D. Isailovic, D.E. Clemmer, Anal. Chem. 79 (2007) 7965.
[47] D. Isailovic, R.T. Kurulugama, M.D. Plasencia, S.T. Stokes, Z. Kyselova, R. Goldman, Y. Mechref, M.V. Novotny, D.E. Clemmer, J. Proteome Res. 7 (2008) 1109.
[48] S. Trimpin, B. Tan, B.C. Bohrer, S.I. Merenbloom, D.E. Clemmer, J.M. Walker, Lipidome profiling with ion mobility spectrometry-mass spectrometry, in: 56th ASMS Conference on Mass Spectrometry, June 1–5, 2008, Denver, CO. Day Code: WOE pm, Session: Lipid Analysis by Mass Spectrometry, Slot 2:50 pm., 2008.
[49] S. Trimpin, B. Tan, D.K. O'Dell, D.E. Clemmer, J.M. Walker, Structures of *N*-Acyl amino acids profiled by ion mobility spectrometry-mass spectrometry, to be submitted.
[50] N.P. Barrera, N. Di Bartolo, P.J. Booth, C.V. Robinson, Science 321 (2008) 243.
[51] M. Rafat, K.W. Fong, A. Goldsipe, B.C. Stephenson, S.T. Coradetti, T.G. Sambandan, A.J. Sinskey, C. Rha, J Colloid Interface Sci. 325 (2008) 324.
[52] G. Giorgi, L. Ceraulo, V.T. Liveri, J. Phys. Chem. B. 112 (2008) 1376.
[53] S.N. Jackson, H.Y. Wang, A.S. Woods, M. Ugarov, T. Egan, J.A. Schultz, J. Am. Soc. Mass Spectrom. 16 (2005) 133.
[54] J.A. Taraszka, A.E. Counterman, D.E. Clemmer, Int. J. Mass Spectrom. 204 (2001) 87.
[55] S. Lee, T. Wyttenbach, G. von Helden, M.T. Bowers, J. Am. Chem. Soc. 117 (1995) 10159.
[56] T. Wyttenbach, G. von Helden, M.T. Bowers, J. Am. Chem. Soc. 118 (1996) 8355.
[57] J. Willmann, K. Mahlstedt, D. Leibfritz, M. Spraul, H. Thiele, Anal. Chem. 79 (2007) 4188.
[58] M.C. Sullards, J.C. Allegood, S. Kelly, E. Wang, C.A. Haynes, H. Park, Y. Chen, A.H. Merrill Jr., Meth. Enzymol. 432 (2007) 83.
[59] F.F. Hsu, J. Turk, J. Am. Soc. Mass Spectrom. 14 (2003) 352.
[60] A.M. McAnoy, C.C. Wu, C. Murphy, Robert, J. Am. Soc. Mass Spectrom. 16 (2005) 1498.
[61] C.S. Ejsing, E. Duchoslav, J. Sampaio, K. Simons, R. Bonner, C. Thiele, K. Ekroos, A. Shevchenko, Anal. Chem. 78 (2006) 6202.
[62] S. Trimpin, M.L. Deinzer, J. Am. Soc. Mass Spectrom. 18 (2007) 1533.
[63] S. Trimpin, M.L. Deinzer, Anal. Chem. 79 (2007) 71.
[64] S. Trimpin, A. Rouhanipour, R. Az, H.J. Räder, K. Müllen, Rapid Commun. Mass Spectrom. 15 (2001) 1364.
[65] S. Trimpin, A.C. Grimsdale, H.J. Räder, K. Müllen, Anal. Chem. 74 (2002)3777.
[66] S. Trimpin, S. Keune, H.J. Räder, K. Müllen, J. Am. Soc. Mass Spectrom. 17 (2006) 661.
[67] S. Trimpin, D.E. Clemmer, J.M. Walker, Lipid Characterization using Total Solvent-free Analysis. Sanibel Conference on Mass Spectrometry by American Society for Mass Spectrometry: "Lipidomics and Lipids in Mass Spectrometry", St. Petersburg Beach, Florida, 2009, January 23–26.